# Super-Resolution Reconstruction of Fetal Brain MRI with Prior Anatomical Knowledge

Shijie Huang[1], Geng Chen[2], Kaicong Sun[1], Zhiming Cui[1], Xukun Zhang[3], Peng Xue[1,4], Xuan Zhang[5], He Zhang[6], and Dinggang Shen[1,7,8(✉)]

[1] School of Biomedical Engineering, ShanghaiTech University, Shanghai 201210, China
dgshen@shanghaitech.edu.cn
[2] National Engineering Laboratory for Integrated Aero-Space-Ground-Ocean Big Data Application Technology, School of Computer Science and Engineering, Northwestern Polytechnical University, Xi'an, China
[3] Academy for Engineering and Technology, Fudan University, Shanghai, China
[4] School of Mechanical, Electrical and Information Engineering, Shandong University, Weihai 264209, China
[5] Department of Radiology, The First Affiliated Hospital of Nanjing Medical University, Nanjing 210000, China
[6] Department of Radiology, Obstetrics and Gynecology Hospital of Fudan University, Shanghai, China
[7] Shanghai United Imaging Intelligence Co., Ltd., Shanghai, China
[8] Shanghai Clinical Research and Trial Center, Shanghai 201210, China

**Abstract.** Super-resolution reconstruction (SRR) of fetal brain MRI from motion-corrupted thick-slice stacks can provide high-resolution isotropic 3D images that are vital for prenatal examination and quantification of brain development. Existing fetal brain SRR methods generally rely on a two-stage optimization procedure by performing rigid *slice-to-volume registration* and *volumetric reconstruction* in an alternating manner. Despite their advantages, these methods have not considered additional guidance from external anatomical priors, resulting in unsatisfactory performance in various challenging cases. To address this issue, we propose a novel **P**rior **A**natomical **K**nowledge guided fetal brain **S**uper-**R**esolution **R**econstruction method, namely **PAK-SRR**. In PAK-SRR, we consider two key kinds of prior anatomical information. First, we integrate the anatomical prior provided by tissue segmentation into both the *slice-to-volume registration* and *volumetric reconstruction* to enforce registration consistency on boundaries, effectively alleviating misregistration caused by blurry tissue boundaries of brain. Second, to enrich the structural details of the reconstructed images, we further employ longitudinal fetal brain atlases to guide *volumetric reconstruction*. Extensive experiments on multi-site clinical datasets demonstrate that our PAK-SRR significantly outperforms the state-of-the-art SRR methods for fetal brain MRI, quantitatively and qualitatively. Our code is publicly available at https://github.com/sj-huang/PAK-SRR for reproducibility and further research.

S. Huang and G. Chen— Contributed equally.


A. Frangi et al. (Eds.): IPMI 2023, LNCS 13939, pp. 428–441, 2023.
https://doi.org/10.1007/978-3-031-34048-2_33

**Keywords:** Fetal Brain · Prior Anatomical Knowledge · Super-Resolution Reconstruction · Brian Tissue Segmentation

## 1 Introduction

Acquiring isotropic high-resolution (HR) magnetic resonance (MR) images from fetal brain is essential for prenatal examination and brain development studies. However, it is clinically difficult to acquire such isotropic HR volumetric images due to large irregular motion of fetal subjects. In this way, fetal brains are often scanned in a short time with fast imaging protocols (e.g., SSFSE: single-shot fast spin echo [4]), which acquire multiple thick-slice stacks from different views, as shown in Fig. 1. These different-view stacks are further integrated using super-resolution reconstruction (SRR) techniques at the post-acquisition stage to obtain desired isotropic HR volumetric images. However, it is challenging to conduct fetal brain SRR due to **1)** poor slice image quality caused by large irregular motion, **2)** misalignment among intra- and inter-stack slices, and **3)** large variation of fetal brains in the acquired MR images [13].

To tackle these challenges, Rousseau *et al.* [13] proposed an approach to reconstruct 3D isotropic HR volumetric images for fetal brain from multi-view (direction) and multi-resolution 2D slices, by iteratively performing *slice-to-volume registration* and *volumetric reconstruction*, after preprocessing of acquired data. Kuklisova-Murgasova *et al.* [9] used expectation-maximization statistics to discard the potential outliers for more robust SRR. Moreover, they applied intensity matching to compensate for the inconsistency of multi-slices. Rousseau *et al.* [14] later improved the regularization procedure associated with SRR to preserve better boundaries. However, these approaches are semi-automatic since fetal brain region needs to be predefined [2]. To resolve this issue, Ebner *et al.* [2] proposed an automatic approach to integrate localization, segmentation, and SRR into a unified framework. Besides, deep learning has been employed to improve the performance of fetal brain SRR [7,15,18]. However, deep learning-based methods rely on large-scale high-quality training data, and suffer from generalization issues, thus limiting their practical applications. Despite the progress of existing methods [2,5,9,13,14,19], they all ignore the use of anatomical prior, which can provide vital information to improve the SRR of fetal brain MRI. This leads to unsatisfactory performance for various challenging cases with large irregular motions and low image quality, as shown in Fig. 1.

To this end, we propose a novel method, namely **PAK-SRR**, to employ rich prior anatomical knowledge (PAK), including tissue segmentation maps (i.e., *seg-priors*) and longitudinal fetal brain atlases (i.e., *atlas-priors*), as strong guidance to improve the SRR of fetal brain MRI (Fig. 1). Specifically, we employ *seg-priors* from tissue segmentation maps to guide more accurate *slice-to-volume registration*, which can improve the quality of reconstructed HR volumetric images. Furthermore, we employ *atlas-priors* (with rich anatomical priors) to address image degradation caused by motion artifacts and thick-slice acquisition. These two kinds of prior anatomical information are integrated into a unified regularization framework, which is optimized by an effective linear least-squares solver,

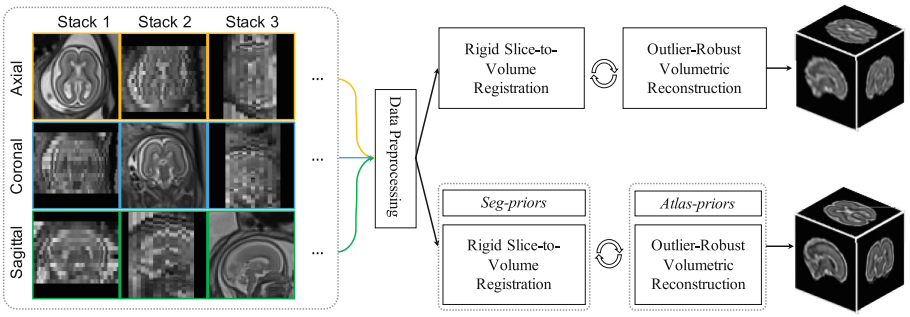


**Fig. 1.** Comparison of the existing framework (right top) [2] with our PAK-SRR (right bottom).

called LSMR [3]. Experimental results on multi-site clinical datasets demonstrate that our PAK-SRR achieves state-of-the-art reconstruction performance along with strong robustness against motion artifacts.

## 2 Background

The SRR of fetal brain MRI utilizes stacks of acquired 2D slices to reconstruct 3D super-resolution image and is usually formulated by the slice acquisition model [5] as below:

$$\mathbf{y}_k = \mathbf{A}_k(\mathbf{x}) + \mathbf{e}_k, \tag{1}$$

where $\mathbf{y}_k$ is the acquired $k_{th}$ slice and $\mathbf{x}$ is the tentative 3D HR image. $\mathbf{A}_k$ is an operator including *slice-to-volume* transformation $\boldsymbol{T}_k$ and blurring operator $\boldsymbol{B}$ (based on a certain point spread function (PSF) [11]). Generally, we can formulate $\mathbf{A}_k(\cdot) := [\boldsymbol{T}_k \circ \boldsymbol{B}(\cdot)]_k$, where the symbol $\circ$ denotes resampling operation, and $[\cdot]_k$ indicates the corresponding plane of the slice $\mathbf{y}_k$ in the 3D image. The vector $\mathbf{e}_k$ represents an additive noise.

Due to the ill-posedness of the above problem in Eq. (1), the commonly used methods for SRR of fetal brain MRI are based on a two-stage iterative registration-reconstruction framework, including 1) *slice-to-volume registration* and 2) *volumetric reconstruction*. In each iteration $i$, *slice-to-volume registration* is performed to align each slice $\mathbf{y}_k$ with the tentatively reconstructed volumetric image $\mathbf{x}$ usually by minimizing the following objective function:

$$\boldsymbol{T}_k^{(i)} = \underset{\boldsymbol{T}_k}{\operatorname{argmin}} \left( \mathcal{S}(\mathbf{x}^{(i-1)}, \mathbf{y}_k; \boldsymbol{T}_k) + \mathcal{R}_{\mathcal{T}}(\boldsymbol{T}_k) \right), \tag{2}$$

where $\mathcal{S}$ represents the similarity measure between slice $\mathbf{y}_k$ and the transformed volume $\mathbf{x}$, and $\mathcal{R}_{\mathcal{T}}(\cdot)$ is the regularization term for the transformation $\boldsymbol{T}_k$. It should be noted that transformation is usually applied on volume $\mathbf{x}$ instead of slice $\mathbf{y}_k$, since resampling a 2D slice in 3D space is not as well defined as sampling a volume. Rigid transformation is usually employed for registration [2,9,13,14], which includes six Degrees of Freedom (DoF) for each individual

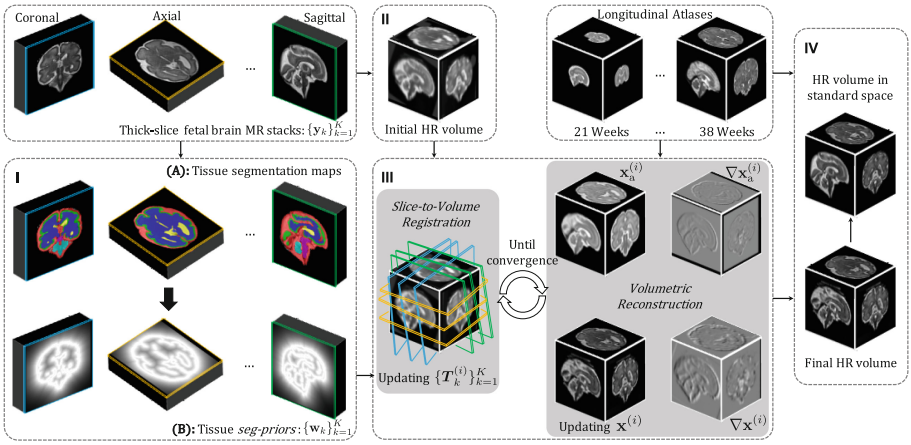


**Fig. 2.** Overview of our proposed PAK-SRR for fetal brain MRI. (I) Extracting brain tissue maps and the corresponding *seg-priors* (i.e., $\{\mathbf{w}_k\}_{k=1}^K$). (II) Aligning multi-view stacks (i.e., $\{\mathbf{y}_k\}_{k=1}^K$) into the same space for obtaining an initial coarse HR volumetric image. (III) The two-stage iterative registration-reconstruction stage, including a *seg-priors* guided *slice-to-volume registration* for updating $\{\boldsymbol{T}_k^{(i)}\}_{k=1}^K$ and a *seg-priors* and *atlas-priors* jointly guided (with $\{\mathbf{w}_k\}_{k=1}^K$ and $\nabla\mathbf{x}_{\mathrm{a}}^{(i)}$) *volumetric reconstruction* for updating $\mathbf{x}^{(i)}$. (IV) Reorienting the final reconstructed 3D image into standard anatomical space defined by longitudinal atlases.

slice. Mathematically, we omit subscript $k$ for clarity and can formulate the transformation as a $4\times4$ matrix $\boldsymbol{T} = \begin{bmatrix} \boldsymbol{R}(\boldsymbol{\theta}) & \boldsymbol{d} \\ 0 & 1 \end{bmatrix}$, where $\boldsymbol{R}(\boldsymbol{\theta})$ denotes a rotation matrix parameterized by three rotational parameters $\boldsymbol{\theta} = (\theta_u, \theta_v, \theta_w)^T$, and $\boldsymbol{d} = (d_u, d_v, d_w)^T$ is a vector of three translation parameters in the 3D space.

*Volumetric reconstruction* is performed when the transformations $\{\boldsymbol{T}_k^{(i)}\}_{k=1}^K$ are updated in each iteration. Assuming $\mathbf{e}_k$ being an additive white Gaussian noise, the image $\mathbf{x}$ can be updated as below:

$$\mathbf{x}^{(i)} = \underset{\mathbf{x}}{\operatorname{argmin}} \left( \sum_k \frac{1}{2} \left\| \mathbf{y}_k - \mathbf{A}_k^{(i)}(\mathbf{x}) \right\|_2^2 + \mathcal{R}_{\mathbf{x}}(\mathbf{x}) \right), \tag{3}$$

where $\mathcal{R}_{\mathbf{x}}(\cdot)$ regularizes the solution space of the latent 3D image $\mathbf{x}$. The optimization problem can be solved by popularly used least-square solver. The above-described two-stage framework performs alternating update of transformations $\{\boldsymbol{T}_k^{(i)}\}_{k=1}^K$ and 3D image $\mathbf{x}^{(i)}$ until convergence.

## 3 Method

An overview of our proposed PAK-SRR is shown in Fig. 2. Different from the existing methods for SRR of fetal brain MRI, we consider two key kinds of prior

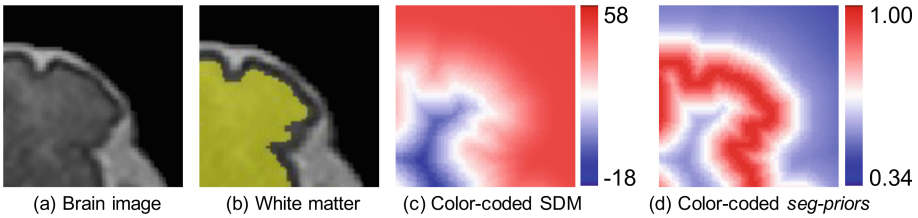


**Fig. 3.** Demonstration of the stages for calculation of the *seg-priors*. (a) Brain image; (b) Segmented white matter; (c) Color-coded SDM for white matter; (d) Color-coded *seg-priors* for white matter. (Color figure online)

anatomical information from **1)** tissue segmentation maps (*seg-priors*) and **2)** longitudinal fetal brain atlases (*atlas-priors*), and integrate them into the two-stage iterative registration-reconstruction framework for improving the registration accuracy and reconstruction performance. The effectiveness of our *seg-priors* and *atlas-priors* will be demonstrated in Sect. 4.

### 3.1 *Slice-to-Volume Registration* Guided by *Seg-priors*

The *slice-to-volume registration* stage aligns multi-resolution and multi-view input slices with the tentatively-reconstructed volume by rigid registration. However, accurate registration is challenging due to large irregular motion and blurry tissue boundaries in the input stacks, which may cause misalignment and result in unsatisfactory SRR. To resolve this issue, we perform tissue segmentation and employ the *seg-priors* to assist the *slice-to-volume registration*. Specially, we perform segmentation for six types of tissues, including cerebrospinal fluid, grey matter, white matter, ventricles, cerebellum, and brainstem. Based on the segmentation results, we calculate the individual Signed Distance Map (SDM) [1] for each of six types of tissues, and then calculate the mean of six SDMs ($N = 6$) as the *seg-priors* $\{\mathbf{w}_k\}_{k=1}^{K}$ as follows:

$$\mathbf{w}_k = \frac{1}{N}\sum_{t=1}^{N} c^{\frac{-\left|SDM_k^{(t)}\right|}{\left\|SDM_k^{(t)}\right\|_\infty}}, \tag{4}$$

where $c$ is a constant used to control the contrast of the map (the larger $c$, the larger the contrast), and in the experiments, we set $c = 1e^3$. The operators $|\cdot|$ and $\|\cdot\|_\infty$ calculate the absolute value and $\ell_\infty$-norm, respectively. The calculation of *seg-priors* for white matter is demonstrated in Fig. 3.

We incorporate the *seg-priors* $\{\mathbf{w}_k\}_{k=1}^{K}$ into the calculation of similarity measure, i.e., normalized cross-correlation coefficient (NCC), and obtain our proposed weighted NCC as

$$\mathrm{NCC}_{\mathbf{w}}(I_1, I_2) := \frac{\sum_j \mathbf{w}^{(j)}\left(I_1^{(j)} - \bar{I}_1\right)\left(I_2^{(j)} - \bar{I}_2\right)}{\sqrt{\sum_j \left(I_1^{(j)} - \bar{I}_1\right)^2}\sqrt{\sum_j \left(I_2^{(j)} - \bar{I}_2\right)^2}}, \tag{5}$$

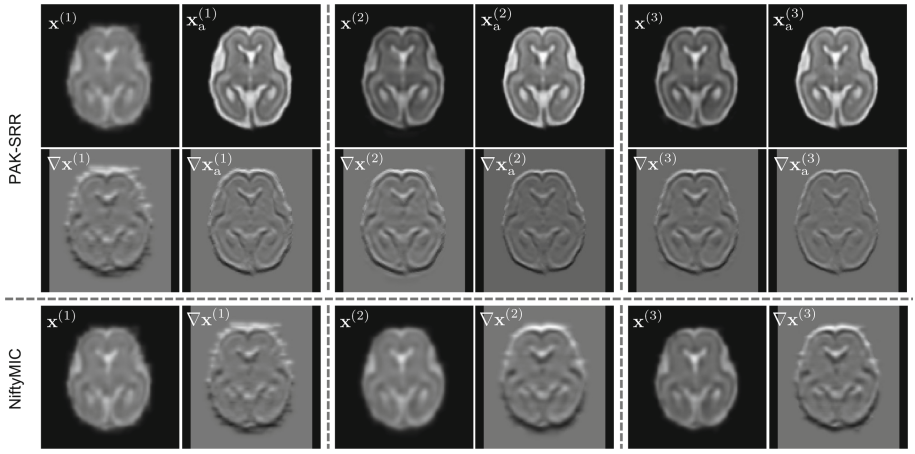


**Fig. 4.** Visualization of the reconstructed volume ($\mathbf{x}^{(i)}$), the registered atlas ($\mathbf{x}_a^{(i)}$), and the corresponding gradient maps ($\nabla\mathbf{x}^{(i)}$ and $\nabla\mathbf{x}_a^{(i)}$) by both methods (shown in first two rows for PAR-SRR, and third row for NiftyMIC) at three update iterations (shown horizontally with two columns for each iteration).

where $I_1$ and $I_2$ denote the vectorized images and $\mathbf{w}$ is the vectorized *seg-priors*. The index $j$ denotes the $j_{th}$ element of the vector. Therefore, we can update the transformation $\boldsymbol{T}_k^{(i)}$ of the $k_{th}$ slice at iteration $i$ with

$$\boldsymbol{T}_k^{(i)} = \underset{\boldsymbol{T}_k}{\operatorname{argmin}} \left( -\mathrm{NCC}_{\mathbf{w}_k}(\mathbf{y}_k, [\boldsymbol{T}_k \circ \boldsymbol{B}(\mathbf{x}^{(i-1)})]_k) \right). \tag{6}$$

In this way, we penalize more on boundary misalignment, and can obtain improved registration performance on boundary areas, which usually convey more structural information and are thus critical for downstream applications.

### 3.2 *Volumetric Reconstruction* Jointly Guided by *Seg-priors* and *Atlas-priors*

The *volumetric reconstruction* stage aims to reconstruct a super-resolution volumetric image based on the aligned thick-slice stacks. In this stage, we intend to employ the *seg-priors* and *atlas-priors* jointly. First, we integrate the calculated *seg-priors* $\{\mathbf{w}_k\}_{k=1}^K$ into the maximum a posteriori (MAP)-based *volumetric reconstruction* stage:

$$\mathbf{x}^{(i)} = \underset{\mathbf{x}}{\operatorname{argmin}} \left( \sum_{k \in \mathscr{K}_\delta^{(i)}} \frac{1}{2} \left\| \mathbf{y}_k - \mathbf{A}_k^{(i)}(\mathbf{x}) \right\|_{\mathbf{w}_k}^2 + \frac{\alpha}{2} \|\nabla \mathbf{x}\|_2^2 \right), \tag{7}$$

where $\|\cdot\|_{\mathbf{w}_k}^2$ represents the weighted $\ell_2$-norm with the weights $\mathbf{w}_k$ being diagonal matrix for the $k_{th}$ slice. Following the work of [2], we eliminate the outlier slices which are severely corrupted by large motion according to the following rule:

$$\mathscr{K}_{\delta}^{(i)} := \left\{ 1 \leq k \leq K : \mathrm{NCC}(\mathbf{y}_k, \mathbf{A}_k^{(i)}(\mathbf{x}^{(i-1)})) \geq \delta \right\}, \tag{8}$$

where $\mathscr{K}_{\delta}^{(i)}$ denotes a set of indices of inlier slices. NCC$(\cdot)$ measures the slice similarity such that the slices with similarity less than a predefined threshold $\delta$ are considered as outliers and will be discarded in the *volumetric reconstruction* stage.

Second, to compensate for the information loss due to motion artifacts, we resort to longitudinal fetal brain atlases and use gradient maps of certain time-point atlases as auxiliary information for *volumetric reconstruction*. In Fig. 4, we demonstrate the gradient maps of a reconstructed volumetric image and the atlas [6]. As can be observed, the atlas usually has sharper boundaries and sharper gradient maps than the initially reconstructed volumetric image, implying that atlas information can be utilized to compensate for blurry boundaries and improve quality of the reconstructed images. Therefore, we register the atlas to the tentatively reconstructed volumetric image, denoted as $\mathbf{x}_{\mathrm{a}}$, and impose similarity match between the gradient of the volume $\nabla\mathbf{x}$ and the corresponding one of the *atlas-priors* (i.e., $\nabla\mathbf{x}_{\mathrm{a}}$) to obtain clearer boundaries in the reconstructed images. Mathematically, we can use the following formulation:

$$\mathbf{x}^{(i)} = \underset{\mathbf{x}}{\operatorname{argmin}} \left( \sum_{k \in \mathscr{K}_{\delta}^{(i)}} \frac{1}{2} \left\| \mathbf{y}_k - \mathbf{A}_k^{(i)}(\mathbf{x}) \right\|_{\mathbf{w}_k}^2 + \frac{\alpha}{2} \|\nabla\mathbf{x} - \varepsilon\nabla\mathbf{x}_{\mathrm{a}}\|_2^2 \right), \tag{9}$$

where $\varepsilon$ and $\alpha$ are scalar parameters. The prior knowledge from the atlases can effectively guide the volumetric reconstruction from low-quality slices. Those slices with severe quality degradation usually decrease reconstruction performance. It is worth noting that, when introducing *atlas-priors* into the regularization, the overall intensities of the reconstructed volumetric image $\mathbf{x}$ might slightly deviate from the input slices during the optimization, as shown in Fig. 4. To alleviate this effect, we perform histogram matching between the tentatively reconstructed volumetric image and its corresponding input stacks during *slice-to-volume registration* in each iteration.

## 4 Experiments

### 4.1 Dataset

We have evaluated our proposed PAK-SRR on fetal brain MRI of 66 subjects covering 20 to 38 gestational weeks (GWs) from multi-site clinic centers, with totally 213 stacks. Each subject was scanned under at least three different-view (direction) stacks by the SSFSE sequence with different spatial resolutions including $1.3 \times 1.3 \times 5$, $1.5 \times 1.5 \times 4.2$, $0.625 \times 0.625 \times 3$, and $0.55 \times 0.55 \times 4.4$ mm. We use bias field correction [8] to preprocess all different-view stacks.

### 4.2 Experimental Settings

We do the following settings for our experiments. **1)** For selecting a target stack used initially to build a tentative HR 3D MR image of each fetal brain, we first

**Table 1.** Quantitative comparison between PAK-SRR and other methods on multi-site datasets of 66 subjects. The best results are in **bold**.

| | Rousseau *et al.* [13] | SVRTK [9] | BTK [14] | NiftyMIC [2] | PAK-SRR |
|---|---|---|---|---|---|
| PSNR | $18.68 \pm 3.81$ | $19.42 \pm 4.55$ | $19.65 \pm 4.31$ | $22.88 \pm 5.44$ | $\mathbf{24.60 \pm 5.19}$ |
| SSIM | $0.7303 \pm 0.1909$ | $0.7074 \pm 0.1907$ | $0.7527 \pm 0.1950$ | $0.7935 \pm 0.2027$ | $\mathbf{0.8401 \pm 0.1412}$ |
| NCC | $0.78 \pm 0.24$ | $0.78 \pm 0.24$ | $0.80 \pm 0.24$ | $0.85 \pm 0.23$ | $\mathbf{0.91 \pm 0.09}$ |

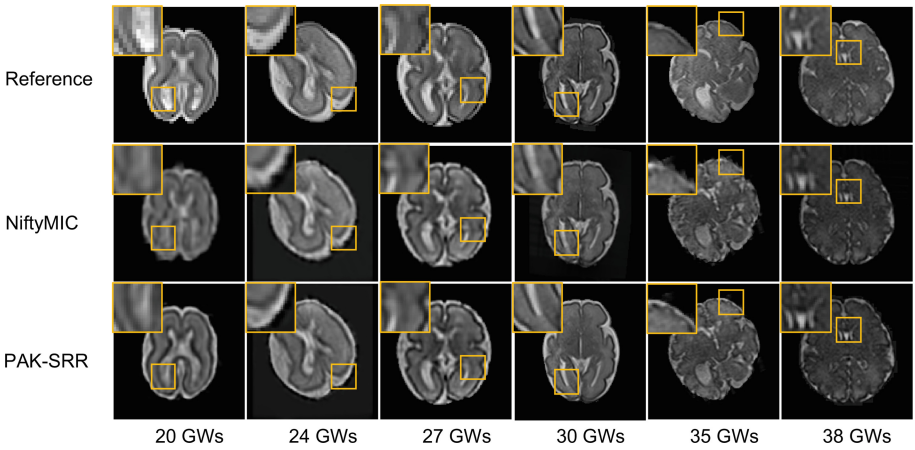


**Fig. 5.** Qualitative results by NiftyMIC and PAK-SRR for subjects at 20, 24, 27, 30, 35, and 38 GWs, shown in 6 columns, respectively.

use U-Net to segment brain tissue map for each different-view stack, and then convert them to *seg-priors* as shown in Fig. 3. Next, we calculate an overlap ratio for each stack with all other stacks according to their respective brain tissue maps. In this way, we can select a stack with the maximum overlap ratio with all other stacks. Finally, by using this selected stack as a target space and aligning all other stacks to it, we can build a tentative HR 3D MR image (for each fetal brain). **2)** For parameters used in Eq. 9, we set the outlier-threshold $\delta$ as 0.6, 0.7, and 0.8, as well as the hyper-parameter $\varepsilon$ as 0.8, 0.7, and 0.6, for the three iterations (for our case of using three iterations), respectively. We set the regularization parameter $\alpha$ to 0.01 for all iterations. **3)** The isotropic resolution for the final HR MR image can be set to a range of 0.5 mm to 1.0 mm. We choose 0.8 mm since the resolution of our employed longitudinal atlases is 0.8 mm (Fig. 5).

### 4.3 Implementation Details

The following pipeline is conducted for all the experiments. **1)** Intensity correction: following the work in [2], we employ linear regression to make intensities of all other stacks consistent with the intensities of the selected target stack. **2)**

**Table 2.** Quantitative results by NiftyMIC and PAK-SRR for normal (N) and abnormal (ABN) subjects from 20 to 38 GWs.

| GWs | # Subjects | NiftyMIC | | | PAK-SRR | | |
|---|---|---|---|---|---|---|---|
| | N:ABN | PSNR | SSIM | NCC | PSNR | SSIM | NCC |
| 20 | 1 : 0 | $20.76 \pm 5.10$ | $0.7778 \pm 0.2013$ | $0.84 \pm 0.20$ | $\mathbf{24.80 \pm 5.12}$ | $\mathbf{0.9201 \pm 0.0467}$ | $\mathbf{0.96 \pm 0.03}$ |
| 24 | 2 : 0 | $21.87 \pm 5.80$ | $0.8001 \pm 0.2062$ | $0.87 \pm 0.20$ | $\mathbf{26.07 \pm 3.61}$ | $\mathbf{0.9226 \pm 0.0624}$ | $\mathbf{0.97 \pm 0.02}$ |
| 27 | 2 : 0 | $21.86 \pm 5.26$ | $0.7975 \pm 0.2125$ | $0.83 \pm 0.25$ | $\mathbf{23.08 \pm 4.90}$ | $\mathbf{0.8658 \pm 0.0909}$ | $\mathbf{0.93 \pm 0.06}$ |
| 30 | 8 : 1 | $22.39 \pm 5.67$ | $0.7922 \pm 0.2025$ | $0.82 \pm 0.24$ | $\mathbf{23.87 \pm 5.49}$ | $\mathbf{0.8536 \pm 0.1201}$ | $\mathbf{0.91 \pm 0.10}$ |
| 31 | 11 : 1 | $20.29 \pm 6.13$ | $0.7197 \pm 0.2383$ | $0.77 \pm 0.29$ | $\mathbf{22.90 \pm 4.30}$ | $\mathbf{0.8166 \pm 0.1361}$ | $\mathbf{0.91 \pm 0.10}$ |
| 32 | 4 : 1 | $24.32 \pm 3.87$ | $0.8691 \pm 0.1000$ | $0.90 \pm 0.16$ | $\mathbf{25.02 \pm 5.11}$ | $\mathbf{0.8700 \pm 0.1078}$ | $\mathbf{0.92 \pm 0.08}$ |
| 33 | 2 : 2 | $23.06 \pm 5.47$ | $0.8094 \pm 0.1853$ | $0.85 \pm 0.23$ | $\mathbf{24.78 \pm 4.89}$ | $\mathbf{0.8709 \pm 0.1076}$ | $\mathbf{0.93 \pm 0.07}$ |
| 34 | 4 : 2 | $23.24 \pm 5.48$ | $0.8072 \pm 0.1985$ | $0.84 \pm 0.25$ | $\mathbf{23.39 \pm 4.91}$ | $\mathbf{0.8333 \pm 0.1282}$ | $\mathbf{0.90 \pm 0.09}$ |
| 35 | 4 : 3 | $23.90 \pm 4.57$ | $0.8342 \pm 0.1566$ | $0.87 \pm 0.20$ | $\mathbf{24.36 \pm 5.39}$ | $\mathbf{0.8455 \pm 0.1331}$ | $\mathbf{0.90 \pm 0.11}$ |
| 36 | 7 : 4 | $23.26 \pm 5.19$ | $0.7618 \pm 0.2340$ | $0.86 \pm 0.21$ | $\mathbf{23.80 \pm 5.54}$ | $\mathbf{0.8006 \pm 0.1979}$ | $\mathbf{0.89 \pm 0.12}$ |
| 37 | 2 : 2 | $26.22 \pm 3.39$ | $0.8761 \pm 0.1062$ | $0.92 \pm 0.14$ | $\mathbf{27.25 \pm 4.26}$ | $\mathbf{0.8988 \pm 0.0751}$ | $\mathbf{0.95 \pm 0.04}$ |
| 38 | 1 : 2 | $23.88 \pm 5.44$ | $0.8106 \pm 0.1605$ | $0.86 \pm 0.21$ | $\mathbf{24.00 \pm 6.08}$ | $\mathbf{0.8124 \pm 0.1479}$ | $\mathbf{0.88 \pm 0.10}$ |

Volume-to-volume rigid registration: we employ the symmetric block-matching algorithm RegAladin [12] to align all stacks with the target stack. **3)** Initial HR volume Estimation: we apply the scattered data approximation approach [2] on the aligned stacks to obtain an initial coarse HR volume. **4)** *Slice-to-volume registration*: our proposed *seg-priors* guided *slice-to-volume registration* algorithm (as described in Sect. 3.1) is used to improve registration accuracy (especially in challenging areas) by introducing tissue *seg-priors*. **5)** *Volumetric reconstruction*: we employ the longitudinal atlases from Gholipour *et al.* [6] and register the corresponding time-point atlas (according to GWs) to the tentatively-estimated HR volume. Based on the guidance of *atlas-priors* (as described in Sect. 3.2), we update the reconstructed HR volume using LSMR algorithm [3]. **6)** Alternatingly optimizing **4)** and **5)** until convergence: the above-described two-stage framework performs the alternating update of transformation $\boldsymbol{T}_k^{(i)}$ and 3D image $\mathbf{x}^{(i)}$ until convergence. **7)** Reorienting HR image: the reconstructed HR volumetric image is further reoriented into the standard anatomical space (defined by longitudinal atlases) for downstream analysis.

### 4.4 Experimental Results

We compare our PAK-SRR with four state-of-the-art methods [2,9,13,14] in terms of peak-signal-to-noise ratio (PSNR), structural similarity index measure [17] (SSIM), and NCC. As shown in Table 1, our PAK-SRR obtains the best mean performance and the best standard deviation in SSIM and NCC. The second-best method, NiftyMIC, outperforms the other three methods also by a large margin. Therefore, in the following experiments, we will focus on the comparison between our PAK-SRR and NiftyMIC.

Table 2 summarizes the statistical results of different GWs for all 66 subjects. We divide the data into normal (clinically defined normal fetal brain growth and

**Table 3.** Quantitative results of NiftyMIC and PAK-SRR for a normal 31 GWs subject under different combinations of input stacks. Note that A, C, and S denote stacks that are acquired with high-resolution in axial, coronal, and sagittal views, respectively.

| Stacks | NiftyMIC | | | PAK-SRR | | |
|---|---|---|---|---|---|---|
| | PSNR | SSIM | NCC | PSNR | SSIM | NCC |
| 3A | $15.34 \pm 4.96$ | $0.5618 \pm 0.2598$ | $0.55 \pm 0.31$ | $\mathbf{20.72 \pm 3.96}$ | $\mathbf{0.7341 \pm 0.1506}$ | $\mathbf{0.77 \pm 0.12}$ |
| 3A+2C | $16.22 \pm 4.80$ | $0.5832 \pm 0.2358$ | $0.62 \pm 0.31$ | $\mathbf{20.80 \pm 3.19}$ | $\mathbf{0.7485 \pm 0.1367}$ | $\mathbf{0.80 \pm 0.10}$ |
| 1A+1C+1S | $18.19 \pm 4.95$ | $0.6966 \pm 0.2094$ | $0.75 \pm 0.24$ | $\mathbf{21.56 \pm 3.23}$ | $\mathbf{0.7941 \pm 0.1088}$ | $\mathbf{0.84 \pm 0.12}$ |
| 3A+2C+2S | $15.58 \pm 4.47$ | $0.5481 \pm 0.3114$ | $0.59 \pm 0.31$ | $\mathbf{20.50 \pm 2.78}$ | $\mathbf{0.7358 \pm 0.1284}$ | $\mathbf{0.79 \pm 0.09}$ |

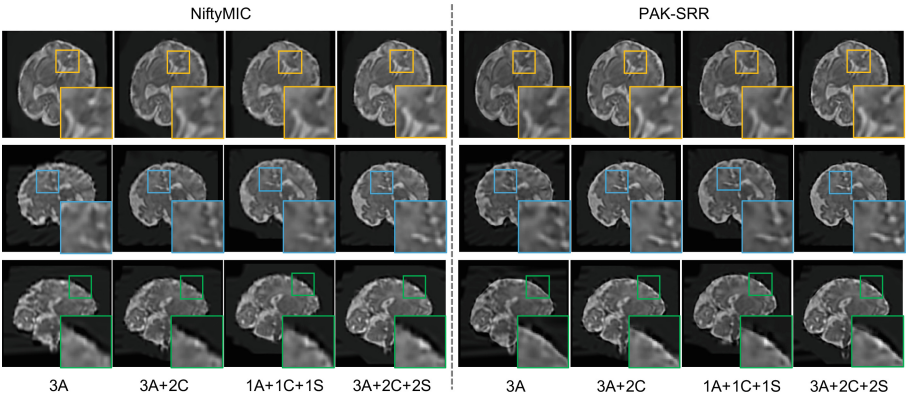


**Fig. 6.** Qualitative results by NiftyMIC and PAK-SRR on 31-GWs subject. A, C, and S denote stacks that are acquired with high-resolution in axial, coronal, and sagittal views, respectively.

development, with appearance close to the atlases) and abnormal (as opposed) cases for better evaluation. As can be observed, for all the cases, our PAK-SRR achieves promising performance in all the evaluation metrics. For the cases mainly containing normal subjects, our proposed PAK-SRR obtains significant improvement over NiftyMIC, especially in SSIM and NCC, which is attributed to the use of additional information from the *atlas-priors*.

For in-depth analysis, we employ different combinations of axial (A), coronal (C), and sagittal (S) views as input to evaluate the effectiveness of our proposed methods. The qualitative performance is illustrated in Fig. 6. It can be seen that NiftyMIC generates blurring boundaries and gets worse when the number of input views reduces. In contrast, PAK-SRR obtains high-quality isotropic images, even using only the axial view from three angles (3A). In fact, in Table 3, we show that, using only 3A views, PAK-SRR generates much better quantitative performance than NiftyMIC using the combinations of all views. Interestingly, the result of 1A+1C+1S outperforms 3A+2C+2S for both methods, indicating that the redundant or possibly-damaged inlier slices may degrade the performance due to misregistration, and another reason might be that the use of more

**Table 4.** Ablation study of key components of our PAK-SRR, ($\mathcal{P}$) denotes the paired t-test p-values for comparison of group means before and after intervention.

| | NiftyMIC | SP-SRR ($\mathcal{P}$) | AP-SRR ($\mathcal{P}$) | PAK-SRR ($\mathcal{P}$) |
|---|---|---|---|---|
| PSNR | $22.88 \pm 5.44$ | $24.26 \pm 5.51$ (2.8e–8) | $24.18 \pm 5.35$ (3.7e–8) | $\mathbf{24.60 \pm 5.19}$ **(1.5e–8)** |
| SSIM | $0.7935 \pm 0.2027$ | $0.8386 \pm 0.1442$ (7.8e–8) | $0.8391 \pm 0.1434$ (6.2e–8) | $\mathbf{0.8401 \pm 0.1412}$ **(5.1e–8)** |
| NCC | $0.85 \pm 0.23$ | $0.89 \pm 0.12$ (1.3e–6) | $0.89 \pm 0.12$ (1.2e–6) | $\mathbf{0.91 \pm 0.09}$ **(1.1e–6)** |

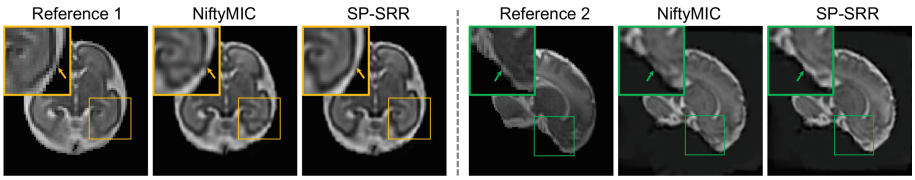


**Fig. 7.** Qualitative performance of NiftyMIC and SP-SRR with the assistance of tissue segmentation in two cases (Left: 27 GWs; Right: 31 GWs).

angular stacks also causes errors in *slice-to-volume registration*. Overall, based on both qualitative and quantitative evaluations, our PAK-SRR achieves much clearer anatomical structures, especially for the challenging samples, and outperforms NiftyMIC for all cases of different GWs and different acquisition views, in terms of all the evaluation metrics.

### 4.5 Ablation Study

In PAK-SRR, we propose two key components, i.e., *seg-priors* (SP) and *atlas-priors* (AP). To demonstrate their effectiveness, we conduct ablation study on two variants, SP-SRR and AP-SRR, for evaluating *seg-priors* and *atlas-priors* (as shown in Table 4), respectively.

**Effectiveness of *Seg-priors*:** The *seg-priors* are obtained by tissue segmentation which is one of the key contributions. Figure 7 demonstrates the results of NiftyMIC and SP-SRR for two fetal brains of 27 GWs and 31 GWs. We can see that both methods obtain reasonable HR images for two fetal brains. However, NiftyMIC reconstructs HR images not only with blurry boundaries but also with less fidelity compared to the reference images. On the contrary, SP-SRR achieves successful reconstruction in these challenging regions as masked and zoomed-up in Fig. 7, demonstrating that the *seg-priors* extracted from the tissue segmentation maps indeed improve both the registration accuracy and the reconstruction performance.

**Effectiveness of *Atlas-priors*:** To show the effectiveness of AP-SRR, we provide a challenging case with large motion and artifacts in Fig. 8. In this case, the brain cannot be identified in the other two views. The NiftyMIC fails to reconstruct the $k_{th}$ slice in the sagittal view, and shows severe streak artifacts in the other two views. In contrast, with the guidance of longitudinal atlases (i.e., *atlas-priors*), AP-SRR achieves promising reconstruction in all three views. It is worth

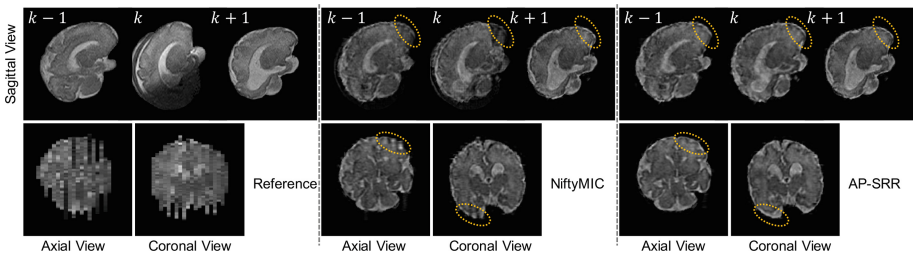


**Fig. 8.** Qualitative performance of NiftyMIC (middle three columns) and AP-SRR (right three columns) for a 35 GWs subject. The $k_{th}$ reference slice of the sagittal view is corrupted with large motion and artifacts (left three column).

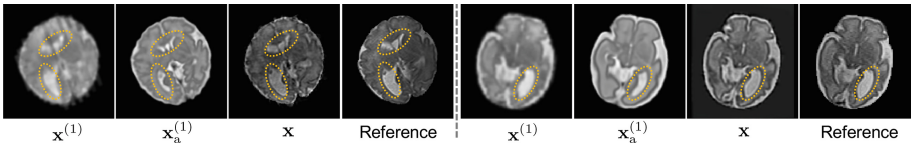


**Fig. 9.** Visualization of the initial image ($\mathbf{x}^{(1)}$), initially-registered atlas ($\mathbf{x}_{\mathrm{a}}^{(1)}$), reconstructed HR image ($\mathbf{x}$), and reference.

noting that since the super-resolved sagittal view provided by AP-SRR intends to compensate for the motion artifact and generates more plausible images than the corrupted input slice, which is usually considered as a reference, it may reduce quantitative assessment for this particular case. In some cases, there might be significant differences between the appearances of the atlas and the reference. Even in this way, the anatomical structures of the reconstructed slices using *atlas-priors* can still be consistent with the references as shown in Fig. 9. This demonstrates the robustness of our proposed method.

## 5 Conclusion

In this paper, we proposed a novel prior-anatomical-knowledge assisted method for super-resolution reconstruction (SRR) of fetal brain MRI, namely PAK-SSR. Our method is built on a two-stage iterative registration-reconstruction scheme. Different from the existing methods, we introduce the *seg-priors*, derived from the segmentation maps of six tissue types in fetal brains, to guide the *slice-to-volume registration* and *volumetric reconstruction*. Moreover, we propose to employ the *atlas-priors*, derived from the longitudinal fetal brain atlases, to exploit developmental characteristics for assisting the *volumetric reconstruction* stage. We performed extensive experiments to evaluate our PAK-SRR. Experimental results show that PAK-SRR outperforms the state-of-the-art SRR methods by a large margin in terms of both quantitative and qualitative evaluations. In the ablation study, we further show that our proposed *seg-priors* and *atlas-priors* can effectively improve *slice-to-volume registration* and *volumetric*

*reconstruction*, eventually providing reconstructed 3D images with high fidelity and clear tissue details. In the future, we will explore to leverage these high-quality fetal brain images to improve existing brain development studies [10,16] by extending the temporal dimension to pro-gestation period.

**Acknowledgement.** This work was supported in part by National Natural Science Foundation of China (grant number 62131015), Science and Technology Commission of Shanghai Municipality (STCSM) (grant number 21010502600), and The Key R&D Program of Guangdong Province, China (grant number 2021B0101420006).

## References

1. Danielsson, P.E.: Euclidean distance mapping. Comput. Graph. Image Process. **14**(3), 227–248 (1980)
2. Ebner, M., et al.: An automated framework for localization, segmentation and super-resolution reconstruction of fetal brain MRI. Neuroimage **206**, 116324 (2020)
3. Fong, D.C.L., Saunders, M.: LSMR: an iterative algorithm for sparse least-squares problems. SIAM J. Sci. Comput. **33**(5), 2950–2971 (2011)
4. Garel, C.: MRI of the Fetal Brain: Normal Development and Cerebral Pathologies. Springer, Heidelberg (2004). https://doi.org/10.1007/978-3-642-18747-6
5. Gholipour, A., Estroff, J.A., Warfield, S.K.: Robust super-resolution volume reconstruction from slice acquisitions: application to fetal brain MRI. IEEE Trans. Med. Imaging **29**(10), 1739–1758 (2010)
6. Gholipour, A., et al.: A normative spatiotemporal MRI atlas of the fetal brain for automatic segmentation and analysis of early brain growth. Sci. Rep. **7**(1), 1–13 (2017)
7. Hou, B., et al.: 3-D reconstruction in canonical co-ordinate space from arbitrarily oriented 2-D images. IEEE Trans. Med. Imaging **37**(8), 1737–1750 (2018)
8. Kim, K., et al.: Bias field inconsistency correction of motion-scattered multislice MRI for improved 3D image reconstruction. IEEE Trans. Med. Imaging **30**(9), 1704–1712 (2011)
9. Kuklisova-Murgasova, M., Quaghebeur, G., Rutherford, M.A., Hajnal, J.V., Schnabel, J.A.: Reconstruction of fetal brain MRI with intensity matching and complete outlier removal. Med. Image Anal. **16**(8), 1550–1564 (2012)
10. Li, G., Nie, J., Wang, L., Shi, F., Lyall, A.E., Lin, W., Gilmore, J.H., Shen, D.: Mapping longitudinal hemispheric structural asymmetries of the human cerebral cortex from birth to 2 years of age. Cereb. Cortex **24**(5), 1289–1300 (2014)
11. Liang, Z.P., Lauterbur, P.C.: Principles of Magnetic Resonance Imaging: A Signal Processing Perspective. "The" Institute of Electrical and Electronics Engineers Press (2000)
12. Modat, M., Cash, D.M., Daga, P., Winston, G.P., Duncan, J.S., Ourselin, S.: Global image registration using a symmetric block-matching approach. J. Med. Imaging **1**(2), 024003 (2014)
13. Rousseau, F., et al.: Registration-based approach for reconstruction of high-resolution in utero fetal MR brain images. Acad. Radiol. **13**(9), 1072–1081 (2006)
14. Rousseau, F., et al.: BTK: an open-source toolkit for fetal brain MR image processing. Comput. Methods Programs Biomed. **109**(1), 65–73 (2013)
15. Shi, W., et al.: AFFIRM: affinity fusion-based framework for iteratively random motion correction of multi-slice fetal brain MRI. IEEE Trans. Med. Imaging (2022)

16. Wang, L., Shi, F., Lin, W., Gilmore, J.H., Shen, D.: Automatic segmentation of neonatal images using convex optimization and coupled level sets. Neuroimage **58**(3), 805–817 (2011)
17. Wang, Z., Bovik, A.C., Sheikh, H.R., Simoncelli, E.P.: Image quality assessment: from error visibility to structural similarity. IEEE Trans. Image Process. **13**(4), 600–612 (2004)
18. Xu, J., Moyer, D., Grant, P.E., Golland, P., Iglesias, J.E., Adalsteinsson, E.: SVoRT: iterative transformer for slice-to-volume registration in fetal brain MRI. In: Wang, L., Dou, Q., Fletcher, P.T., Speidel, S., Li, S. (eds.) Medical Image Computing and Computer Assisted Intervention (MICCAI 2022). LNCS, vol. 13436, pp. 3–13. Springer, Cham (2022). https://doi.org/10.1007/978-3-031-16446-0_1
19. Zhao, C., Dewey, B.E., Pham, D.L., Calabresi, P.A., Reich, D.S., Prince, J.L.: SMORE: a self-supervised anti-aliasing and super-resolution algorithm for MRI using deep learning. IEEE Trans. Med. Imaging **40**(3), 805–817 (2020)